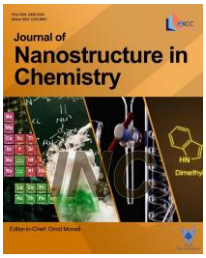

J. Nanostruct Chem. 2026; 16(4): 393-409

Journal of Nanostructure in Chemistry (JNSC)

https://doi.org/10.57647/jnsc.2026.1604.20

Research Article

A Eu-MOF Nanoarchitectured Electrochemiluminescent Sandwich Immunosensor for ProGRP Quantification in Serum and Pleural Effusion

Linlin Luo[1], Chao Xu[2], Sicong Jiang[1], Yuxuan Xing[3], Zhiqian Zhao[4], Shuo Li[5,*]

[1] *The Second Department of Respiratory Disease, Jiangxi Provincial People's Hospital (The First Affiliated Hospital of Nanchang Medical College), Nanchang, 330006, Jiangxi Province, China*
[2] *Department of Orthopedics, Shangrao Municipal Hospital (Affiliated Shangrao Municipal Hospital of Nanchang Medical College), Shangrao, 334000, China*
[3] *Department of Thoracic Surgery, The First Affiliated Hospital of Soochow University, Suzhou, 215006, China*
[4] *Department of Thoracic Surgery, The First Affiliated Hospital of Zhengzhou University, Zhengzhou University, Zhengzhou, 450000, China*
[5] *Department of Respiratory Medicine, The First Affiliated Hospital of Shandong First Medical University & Shandong Provincial Qianfoshan Hospital, Shandong Institute of Respiratory Diseases, Featured Laboratory of Respiratory Immunology and Regenerative Medicine in Universities of Shandong, Jinan Clinical Research Center for Respiratory Disease, Jinan 250014, China*

* **Corresponding authors:** 3228@sdhospital.com.cn

Article History:

Received:
22 February 2026

Revised:
4 April 2026

Accepted:
1 May 2026

Published in Issue:
31 August 2026

Abstract

Effective clinical management of small cell lung cancer (SCLC) requires sensitive and matrix-tolerant quantification of pro-gastrin-releasing peptide (ProGRP). Herein, we report a nanoarchitectured electrochemiluminescence (ECL) sandwich immunosensor that combines a three-dimensional reduced graphene oxide/gold (3D-rGO@Au) capture interface with a luminescent europium metal-organic framework (Eu-MOF) signal probe labeled with Ab2 for ProGRP measurement in serum and pleural effusion. The Eu-MOF formed uniform octahedral particles and provided efficient antenna-effect-assisted ECL emission with $K_2S_2O_8$ as the coreactant, while the 3D-rGO@Au interface increased antibody loading and accelerated interfacial electron transfer. The assay achieved a detection limit of 0.035 pg mL^{-1} over a broad linear range, showed satisfactory recovery in two clinical matrices, and agreed well with commercial ECLIA measurements. Beyond combining two previously reported material families, the main contribution of this work is the clinically oriented integration of a high-loading conductive interface, a Eu-MOF luminophore probe, mechanistic ECL/CV/EIS validation, and real-sample verification for ProGRP detection.

Keywords: Clinical correlation; 3D-rGO@Au interface; Persulfate coreactant; Small cell lung cancer; Spike-and-recovery

Cite this article: Linlin L., Chao X., Sicong J., Yuxuan X., Zhiqian Zh., Shuo L. A Eu-MOF Nanoarchitectured Electrochemiluminescent Sandwich Immunosensor for ProGRP Quantification in Serum and Pleural Effusion. *J Nanostruct Chem* **16**, 393-409 (2026).
https://doi.org/10.57647/jnsc.2026.1604.20

1. Introduction

Mortality associated with malignancies is most frequently driven by lung cancer on a global scale, with small cell lung cancer (SCLC) representing approximately 15% of lung cancers and remaining strongly associated with rapid dissemination and poor prognosis [1-3]. Distinctive features of SCLC include an aggressive clinical course and a high likelihood of early-stage metastasis, culminating in a bleak prognosis in the absence of timely

identification. Therefore, the development of sensitive and reliable methods for the early detection and monitoring of SCLC is of paramount clinical importance. For the identification of SCLC, pro-gastrin-releasing peptide (ProGRP) has been identified as a highly specific and promising diagnostic indicator [1-2, 4]. Unlike other biomarkers such as neuron-specific enolase (NSE), the diagnostic utility of ProGRP is enhanced by its superior specificity, rendering it a critical instrument for monitoring treatment efficacy and performing differential diagnoses [5]. ProGRP can be detected in various biological fluids, including serum and pleural effusion, where its concentration levels demonstrate a robust correlation with SCLC progression and presence [6-8]. However, the clinical utility of ProGRP is often hampered by its susceptibility to degradation within biological environments and the technical difficulties of achieving precise measurement when concentrations are minimal [9-10].

Traditional analytical techniques, specifically radioimmunoassay (RIA) and enzyme-linked immunosorbent assay (ELISA), have seen extensive application for ProGRP screening; nonetheless, they are plagued by constraints such as prolonged processing durations, intricate workflows, inadequate sensitivity, and, regarding RIA, the necessity of radioactive tracers [11-12]. In recent years, although sensitivity has been bolstered by the advent of chemiluminescence immunoassay (CLIA) [13-14], there is still a pressing need for ultrasensitive detection platforms that can quantify trace amounts of ProGRP for early diagnosis and minimal residual disease monitoring. As a potent analytical methodology, electrochemiluminescence (ECL) has attracted substantial scientific interest by merging the benefits inherent to both chemiluminescence and electrochemical processes [15-16]. The development of sophisticated biosensors finds an optimal foundation in ECL, which provides meticulous reaction control via potential modulation, minimal background interference, an expansive dynamic range, and remarkably high sensitivity [15–17].

Recent progress in ProGRP sensing has confirmed the feasibility of electrochemical and ECL strategies, but several practical gaps remain. Reported electrochemical systems based on 3D-rGO@Au or α-Fe_2O_3/Fe_3O_4 nanointerfaces have improved sensitivity, and ECL systems using TiO_2-containing electrodes or Eu-MOF luminophores have expanded optical readout options [17-21]. However, many platforms are still evaluated mainly in buffer, provide limited explanation of interfacial charge transfer, or do not test both serum and pleural-effusion matrices. These issues restrict the translation of high-sensitivity sensors into clinically relevant sample environments. High-performance ECL immunosensors depend not only on low-background electrochemical readout but also on luminophores with efficient excited-state generation and structural stability. Lanthanide-based MOFs, especially Eu-MOFs, are attractive in this context because the Eu(III) centers exhibit narrow emission bands, long excited-state lifetimes, and excellent photostability, while the coordinated organic ligands can act as antenna donors that harvest excitation energy and funnel it toward the emissive Eu(III) core. Compared with simple Eu^{3+} salts, the rigid MOF framework can suppress vibrational quenching, promote ordered energy transfer, and provide a high-density platform for bioconjugation [22-30]. The aqueous and structural stability reported for europium-based MOFs in related sensing studies also supports their suitability as durable signal carriers in analytical systems [31-32]. These characteristics have enabled Eu-MOFs to function as effective ECL probes in biomarker-oriented sensing systems, but for ProGRP detection the literature remains limited and mechanistic controls are still scarce.

A meticulously engineered electrode interface and a dependable strategy for signal amplification are indispensable requirements for the assembly of an immunosensor that is both sensitive and robust. The sandwich-type immunoassay configuration, which utilizes a pair of antibodies (capture and detection) to bind to different epitopes of the target antigen, offers high specificity and reliability [33]. Regarding the electrode substrate, three-dimensional nanostructures exemplified by gold nanoparticle-decorated reduced graphene oxide (3D-rGO@Au), provide a scaffold characterized by accelerated electron transfer kinetics and an expansive surface area for antibody anchoring, thereby optimizing the functional output of the sensor [34]. In terms of signal generation, the development of a potent ECL probe is achieved by integrating Eu-MOF nanoparticles with the detection antibody, facilitating the production of a robust signal that correlates linearly with the quantity of sequestered antigen.

In this work, we developed a mechanistically supported ECL sandwich immunosensor for ultra-trace ProGRP quantification in human serum and pleural effusion. The novelty of this study therefore lies not in claiming a new standalone synthetic route for either 3D-rGO@Au or Eu-MOF, but in coupling a high-loading 3D-rGO@Au capture interface with a Eu-MOF-Ab2 luminophore probe and validating the resulting sandwich ECL architecture in clinically relevant matrices. In addition to analytical calibration, we evaluated PBS stability of the Eu-MOF framework, antibody loading on the electrode and signal probe, CV/EIS evolution during assembly, selectivity against lung-cancer-related biomarkers, recovery in serum and pleural effusion, and agreement with commercial ECLIA. This design provides a clearer analytical rationale for using Eu-MOF-based ECL readout in ProGRP detection.

10.57647/jnsc.2026.1604.20

2. Materials and Methods

2.1. Synthesis of Eu-MOF Nanoparticles

Eu-MOF nanoparticles were prepared by a solvothermal method adapted from Eu-BTC coordination frameworks [35,36]. Briefly, $Eu(NO_3)_3 \cdot 6H_2O$ (133.8 mg, 0.3 mmol) and H_3BTC (70.0 mg, 0.33 mmol) were dissolved in 20 mL of a DMF/ethanol mixed solvent (1:1, v/v), followed by sonication for 30 min to obtain a clear precursor solution. The solution was transferred to a 50 mL Teflon-lined autoclave and heated at 120 °C for 24 h. After natural cooling, the precipitate was collected by centrifugation, washed three times with ethanol and deionized water, and dried under vacuum at 60 °C. This procedure yielded white Eu-MOF nanoparticles that were subsequently used for antibody conjugation.

2.2. Preparation of 3D-rGO@Au Nanocomposite

The 3D-rGO@Au nanocomposite was prepared by adapting reported hydrothermal routes for graphene/Au nanostructures and recent graphene-oxide oxidation protocols [33,34,37,38]. Graphene oxide (GO) was first obtained from graphite powder using an improved oxidation procedure. A 10 mL GO dispersion (2 mg/mL) was then mixed with 1 mL $HAuCl_4$ (10 mM) and heated at 180 °C for 12 h. During this process, GO sheets were reduced and assembled into a porous three-dimensional reduced graphene oxide (rGO) hydrogel, while Au^{3+} was reduced in situ to Au nanoparticles anchored across the rGO network. The product was rinsed thoroughly with water, freeze-dried, and redispersed before electrode modification.

2.3. Fabrication of the ECL Immunosensor

The initial preparation involved the sequential polishing of the bare GCE using 0.3 and 0.05 μm alumina slurries, which was followed by ultrasonic cleaning in both deionized water and ethanol. A gentle stream of nitrogen was then used to dry the purified GCE. To initiate the platform construction, the GCE surface was modified via drop-casting with 5 μL of a 1.0 mg/mL aqueous dispersion of 3D-rGO@Au. The modified 3D-rGO@Au/GCE subsequently underwent an overnight incubation at 4 °C with 10 μL of a 20 μg/mL capture antibody (Ab1) solution prepared in PBS (pH 7.4). The formation of Au-N bonds facilitates the covalent attachment of the Ab1 to the AuNPs. After a brief PBS rinse, the electrode was subjected to a 1-hour immersion in 1% BSA solution at 37 °C, a step designed to block residual active sites and mitigate non-specific adsorption effects. Designated as BSA/Ab1/3D-rGO@Au/GCE, the completed immunosensor was kept at 4 °C for storage.

2.4. Preparation of Eu-MOF-Ab2 Signal Probe

The creation of the ECL signal probe involved the bioconjugation of detection antibodies (Ab2) onto Eu-MOF nanoparticles. The initial stage required the activation of surface carboxyl groups present on the Eu-MOF matrix. In brief, a dispersion was formed by adding 5 mg of Eu-MOF to 1 mL of PBS (pH 7.4), which was then treated with 100 μL of EDC (10 mg/mL) and 100 μL of NHS (10 mg/mL). At ambient temperature, the blend was subjected to gentle agitation for 30 min. Post-activation, centrifugation and PBS washing steps were performed to eliminate surplus EDC and NHS. The modified Eu-MOF was subsequently reconstituted in 1 mL of PBS and combined with 100 μL of Ab2 solution (100 μg/mL). This bioconjugation was maintained for 4 hours at room temperature under mild shaking conditions. To conclude, the synthesized Eu-MOF-Ab2 conjugate was isolated via centrifugation, purified using PBS containing 0.5% BSA, and finally maintained in 1 mL of storage buffer (PBS with 1% BSA) at 4 °C.

2.5. ECL Measurement Procedure

The quantification of ProGRP was performed using a sandwich immunoassay format. The prepared immunosensor (BSA/Ab1/3D-rGO@Au/GCE) was incubated with 10 μL of ProGRP standard solution or clinical sample at various concentrations for 45 min at 37 °C. After rinsing with PBS, the electrode was further incubated with 10 μL of the Eu-MOF-Ab2 probe dispersion (0.5 mg/mL) for another 45 min at 37 °C to form the sandwich immunocomplex. Following a final rinse with PBS, the electrode was transferred to the ECL detection cell containing 10 mL of 0.1 M PBS (pH 7.4) with 0.1 M $K_2S_2O_8$ as the coreactant.

2.6. Clinical Sample Analysis

A total of 50 serum samples and 30 pleural effusion samples were obtained as de-identified residual clinical specimens from the First Affiliated Hospital of Nanchang University after routine diagnostic testing. The serum cohort included 30 patients with pathologically confirmed SCLC (mean age 63.4 ± 8.1 years; 22 males and 8 females) and 20 controls with either benign pulmonary disease or health-screening status (mean age 58.9 ± 9.4 years; 13 males and 7 females). The pleural-effusion cohort included 20 SCLC-associated malignant effusion samples (mean age 64.1 ± 7.6 years; 15 males and 5 females) and 10 non-malignant control effusions (mean age 56.8 ± 10.1 years; 6 males and 4 females). Written informed consent for the use of remnant specimens was obtained according to institutional policy, and the study protocol was approved by the institutional ethics

10.57647/jnsc.2026.1604.20

committee (ethics approval ID: 2026-S357). Samples were centrifuged to remove particulates, aliquoted, and stored at -80 °C. Immediately before measurement, serum was diluted 10-fold to reduce protein-matrix effects and to place high-ProGRP clinical specimens within the linear range, whereas pleural effusion was diluted 5-fold because of its higher baseline viscosity and broader endogenous concentration distribution. Comparative measurements were performed with both the proposed immunosensor and a commercial Roche Elecsys ProGRP ECLIA kit on a Cobas e601 analyzer.

2.7. Instrumentation and Characterization

The morphology of Eu-MOF and 3D-rGO@Au was examined by scanning electron microscopy (SEM) and transmission electron microscopy (TEM). Crystallographic features were analyzed by powder X-ray diffraction (XRD) using Cu Kα radiation, and coordination chemistry was assessed by Fourier-transform infrared spectroscopy (FTIR, 4000-400 cm^{-1}). X-ray photoelectron spectroscopy (XPS, Al Kα radiation) was used to determine surface elemental states. Ultraviolet-visible spectroscopy (UV-vis), dynamic light scattering (DLS), and zeta-potential measurements were used to follow colloidal size and antibody conjugation. Nitrogen adsorption-desorption measurements at 77 K provided Brunauer-Emmett-Teller (BET) surface area and pore-volume values, and thermogravimetric analysis (TGA) was performed under nitrogen at 10 °C min^{-1}. Cyclic voltammetry (CV) and electrochemical impedance spectroscopy (EIS) were conducted in 5.0 mM $[Fe(CN)_6]^{3-/4-}$ containing 0.1 M KCl with a conventional three-electrode system composed of the modified glassy carbon electrode (GCE), an Ag/AgCl reference electrode, and a platinum counter electrode. EIS was recorded over 0.1 Hz-100 kHz with a 5 mV perturbation, and ECL measurements were performed in 0.1 M PBS (pH 7.4) containing 0.1 M $K_2S_2O_8$.

3. Results and Discussion

3.1. Characterization of Synthesized Nanomaterials

The analytical performance of the immunosensor depends strongly on the morphology and structural integrity of the prepared nanomaterials. SEM and TEM images (Fig. 1A and 1B) show that the solvothermal reaction produced uniform Eu-MOF octahedra with clear crystal boundaries and an average size of approximately 110 ± 15 nm. The compact particle shape observed by TEM, together with the HRTEM and SAED results, indicates that the Eu-BTC coordination framework formed with good crystallinity rather than as an amorphous precipitate.

XRD further confirmed the crystalline Eu-MOF framework (Fig. 2A). The main diffraction peaks at 2θ values of 8.9 degrees, 10.3 degrees, 12.8 degrees, 15.5 degrees, and 18.0 degrees are consistent with reported lanthanide-BTC structures [39]. The absence of additional peaks assignable to Eu_2O_3 or free H_3BTC supports the phase purity of the product and agrees with the ordered morphology observed by electron microscopy.

FTIR spectroscopy was used to verify coordination between H_3BTC and Eu(III) (Fig. 2B). Free H_3BTC showed a broad O-H band near 3000 cm^{-1} and a carboxylic C=O vibration around 1715 cm^{-1}. After Eu-MOF formation, the C=O band weakened and new asymmetric and symmetric carboxylate bands appeared at 1605 and 1390 cm^{-1}, respectively. The separation between these bands indicates coordination of carboxylate groups to Eu(III), confirming successful framework assembly [40].

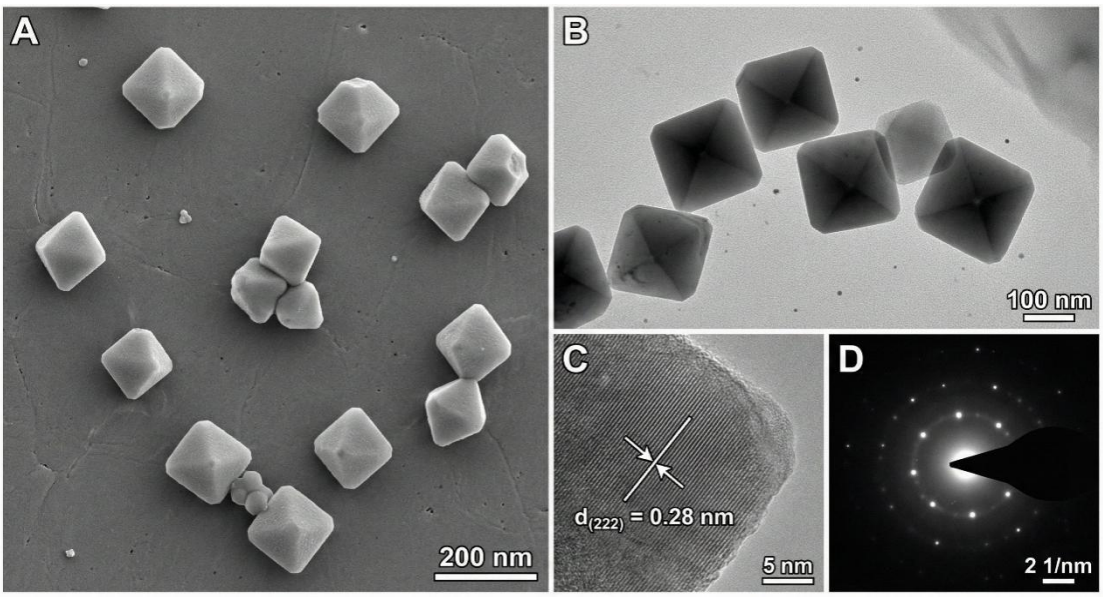

Figure 1. (A) SEM image, (B) TEM image, (C) HRTEM image, and (D) SAED pattern of Eu-MOF crystals

10.57647/jnsc.2026.1604.20

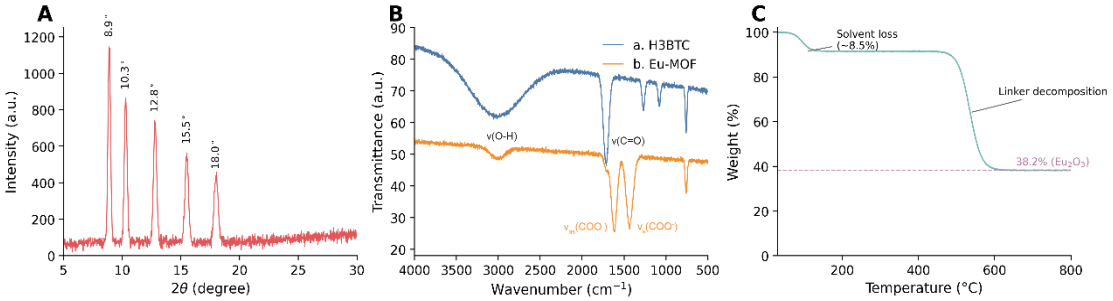

Figure 2. (A) XRD pattern of Eu-MOF nanoparticles. (B) TIR spectra confirming coordination between Eu(III) and the H_3BTC linker. (C) TGA of Eu-MOF nanoparticles under N_2

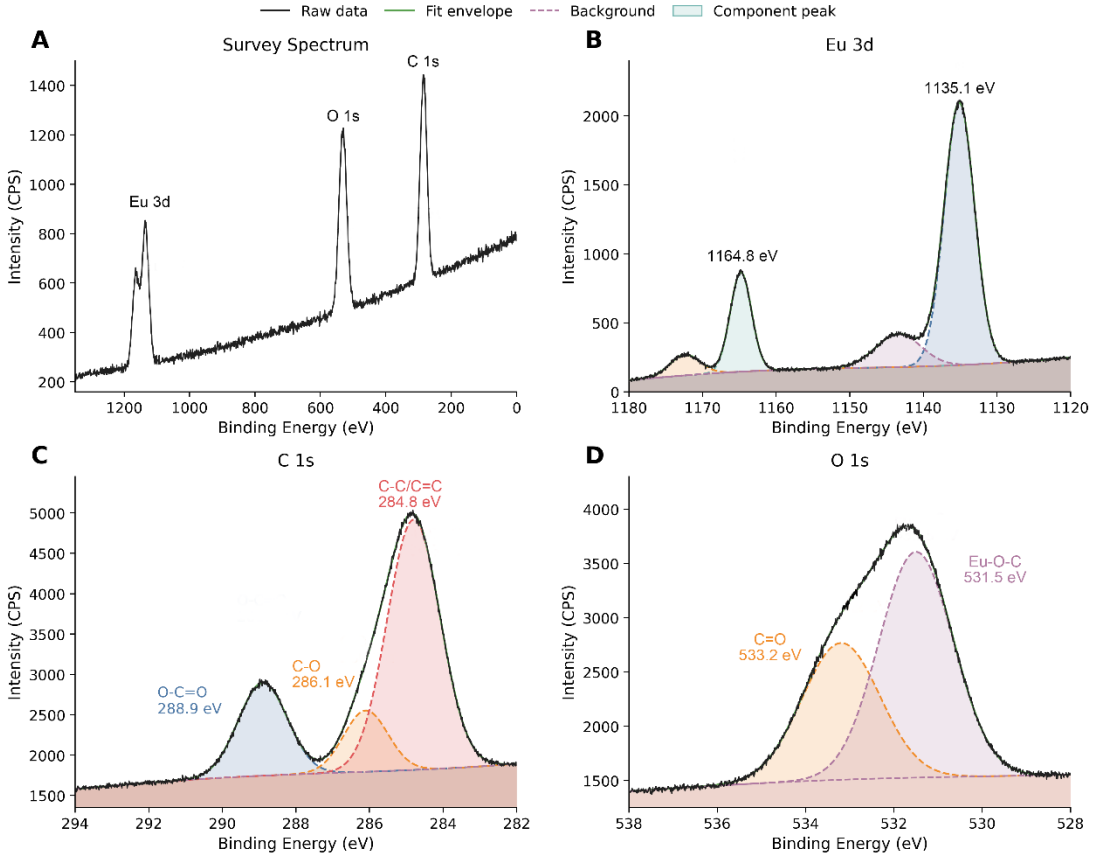

Figure 3. (A) Survey spectrum confirming the presence of Eu, O, and C. (B) High-resolution Eu 3d spectrum. (C) High-resolution C 1s spectrum. (D) High-resolution O 1s spectrum

TGA was performed to evaluate the thermal robustness of the Eu-MOF particles (Fig. 2C). The first mass loss below 150 °C was attributed to removal of guest DMF/ethanol and adsorbed water. The framework remained comparatively stable until approximately 450 °C, after which rapid mass loss reflected decomposition of the organic linker and collapse of the coordination network. This thermal profile is consistent with a solvent-containing Eu-BTC framework rather than loosely adsorbed ligand aggregates.

XPS analysis provided additional evidence for the chemical composition of the Eu-MOF surface. The survey spectrum (Fig. 3A) confirmed the presence of C, O, and Eu. In the Eu 3d region (Fig. 3B), peaks at 1135.1 and 1164.8 eV correspond to Eu 3d5/2 and Eu 3d3/2, supporting the Eu(III) oxidation state. The C 1s and O 1s spectra further showed signals associated with aromatic carbon and coordinated carboxylate groups, in agreement with the FTIR results.

N_2 adsorption-desorption analysis showed that the Eu-MOF possesses a microporous framework (Fig. 4). The measured BET surface area of 1187 $m^2\ g^{-1}$ and pore volume of 0.54 $cm^3\ g^{-1}$ provide abundant accessible sites for probe functionalization and facilitate contact between the luminophore and the aqueous coreactant. Such porosity is advantageous for biosensing because it increases the effective loading capacity of the Eu-MOF-Ab2 signal probe.

10.57647/jnsc.2026.1604.20

The efficacy of the Eu-MOF as an ECL luminophore is primarily dictated by its luminescence characteristics. Fig. 5A presents the emission and photoluminescence (PL) excitation profiles of the Eu-MOF in aqueous dispersion. Upon excitation at 295 nm, the material displays the distinct, narrow emission signatures of Eu(III) ions at 579, 592, 615, 651, and 698 nm, which are assigned to the $^5D_0 \rightarrow {}^7F_n$ (n = 0, 1, 2, 3, 4) transitions, respectively [41–43].

The hypersensitive $^5D_0 \rightarrow {}^7F_2$ transition at 615 nm constitutes the most prominent peak and generates the characteristic intense red emission. When monitoring at 615 nm, the excitation spectrum reveals a broad band peak at 295 nm; this feature is characteristic of the H_3BTC organic linker and does not originate from the Eu(III) ion itself. This observation provides conclusive evidence that the luminescence process is driven by the "antenna effect," where energy is efficiently channeled from the excited ligand to the central Eu(III) emitter [43]. Utilizing an integrating sphere method, the photoluminescence quantum yield (PLQY) of the Eu-MOF was determined to be 68.5%, reflecting superior luminescence efficiency [34].

Furthermore, the luminescence decay kinetics of the Eu-MOF were analyzed. The decay profile for the $^5D_0$ excited state (monitored at 615 nm) is illustrated in Fig. 5B. The data is accurately described by a single exponential decay model, resulting in a calculated lifetime (τ) of 1.25 ms. Such an extended lifetime is a hallmark of lanthanide-based emission and is highly beneficial for time-resolved sensing, as it allows for the effective suppression of background signal interference.

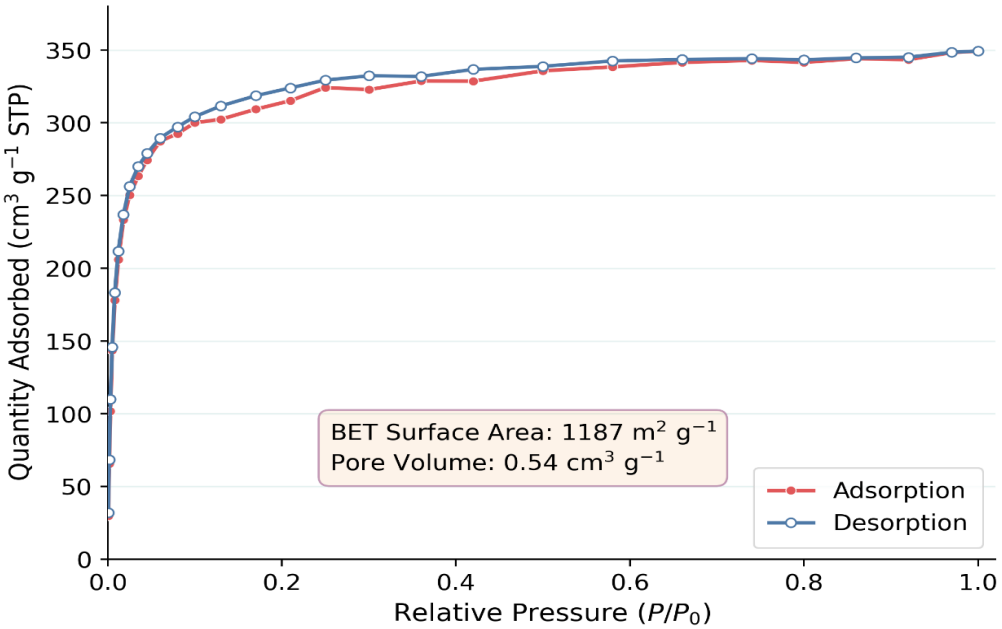

Figure 4. Porosity characterization of Eu-MOF nanoparticles by N_2 adsorption–desorption

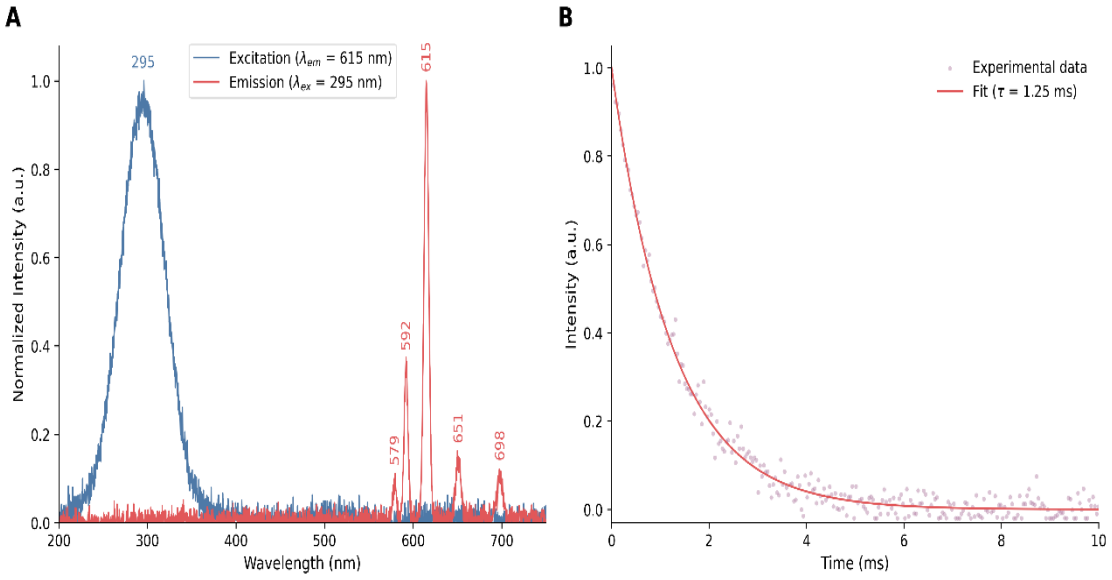

Figure 5. (A) PL excitation (monitored at 615 nm) and emission spectra. (B) Luminescence decay curve monitored at 615 nm fitted to a single-exponential function

10.57647/jnsc.2026.1604.20

SEM images of the 3D-rGO@Au nanocomposite reveal an interconnected porous rGO network decorated with uniformly distributed Au nanoparticles (Fig. 6A). This architecture is beneficial for electrode modification because the open rGO framework promotes mass transport and the Au nanoparticles provide conductive anchoring sites for capture-antibody immobilization. EDX and elemental mapping (Fig. 6B, C) confirm the homogeneous distribution of C, O, and Au, supporting successful in situ growth of Au nanoparticles within the rGO scaffold [45-47].

The successful conjugation of the detection antibody (Ab2) to the Eu-MOF nanoparticles was confirmed by UV-vis spectroscopy and DLS. As shown in Fig. 7A, the Eu-MOF exhibits a characteristic absorption peak at 295 nm, corresponding to the H_3BTC ligand. The Ab2 antibody shows a typical protein absorption peak at 280 nm. After conjugation, the spectrum of Eu-MOF-Ab2 displays both absorption peaks, at 280 nm and 295 nm, providing initial evidence of successful conjugation [44-45]. DLS measurements (Fig. 7B) showed that the average hydrodynamic diameter increased from 135 nm for the bare Eu-MOF to 168 nm for the Eu-MOF-Ab2 conjugate. This increase in size is consistent with the attachment of antibody molecules to the surface of the nanoparticles, further confirming the successful preparation of the signal probe. The zeta potential also shifted from -25.3 mV for Eu-MOF to -18.7 mV for Eu-MOF-Ab2, reflecting the change in surface charge upon protein conjugation. To better quantify bioconjugation efficiency, the antibody-loading capacity of the signal and capture interfaces was estimated from the depletion of protein in the supernatant after conjugation. The Eu-MOF probe immobilized 146 ± 9 μg antibody per mg of MOF, while the 3D-rGO@Au-modified electrode immobilized 1.84 ± 0.12 μg cm^{-2} of capture antibody under the selected conditions. After storage at 4 °C for 14 days, the Eu-MOF-Ab2 dispersion retained 90.7% of its initial ECL response, indicating that the conjugated probe remained sufficiently stable during the analytical window used in this study.

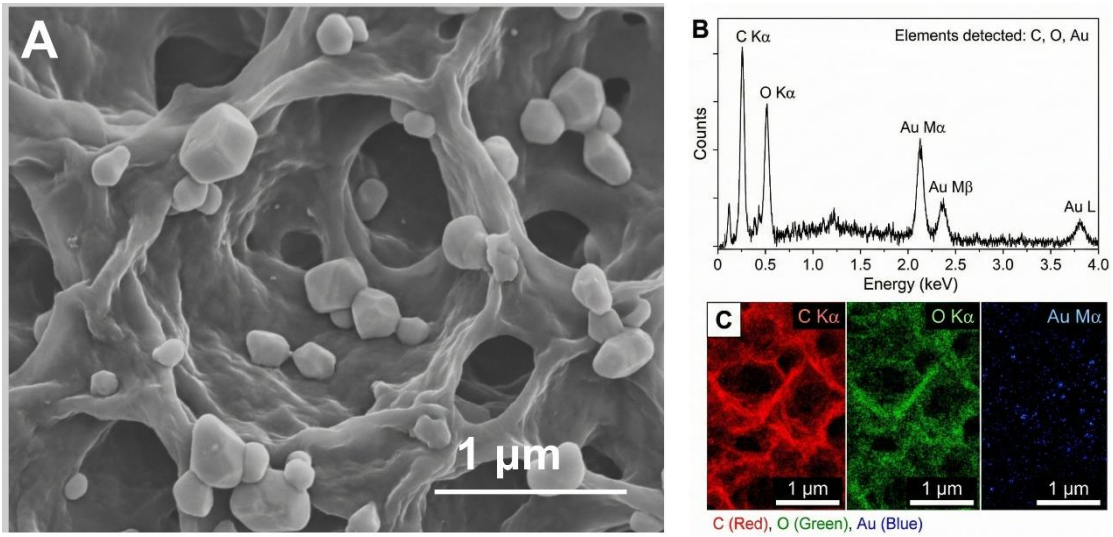

Figure 6. (A) SEM image showing an interconnected, porous three-dimensional reduced graphene oxide (rGO) network decorated with uniformly distributed Au nanoparticles (AuNPs). (B) Energy-dispersive X-ray (EDX) spectrum confirming elemental composition. (C) Elemental mapping images demonstrating homogeneous distribution of C, O, and Au across the nanocomposite, validating successful synthesis of 3D-rGO@Au

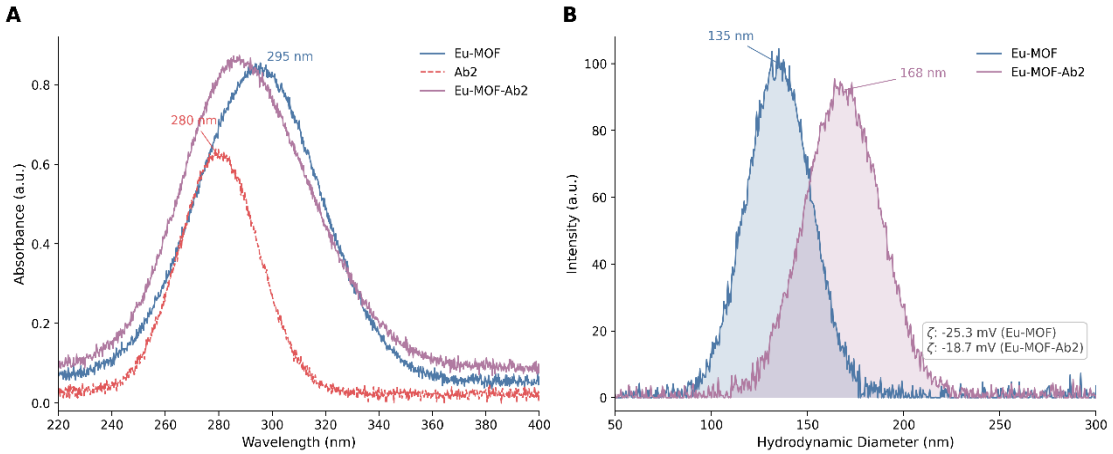

Figure 7. (A) UV–vis absorption spectra of Eu-MOF, Ab2, and Eu-MOF–Ab2. (B) DLS results showing an increase in hydrodynamic diameter from 135 nm (Eu-MOF) to 168 nm (Eu-MOF–Ab2); accompanying zeta potential shift from −25.3 mV to −18.7 mV further supports antibody attachment

10.57647/jnsc.2026.1604.20

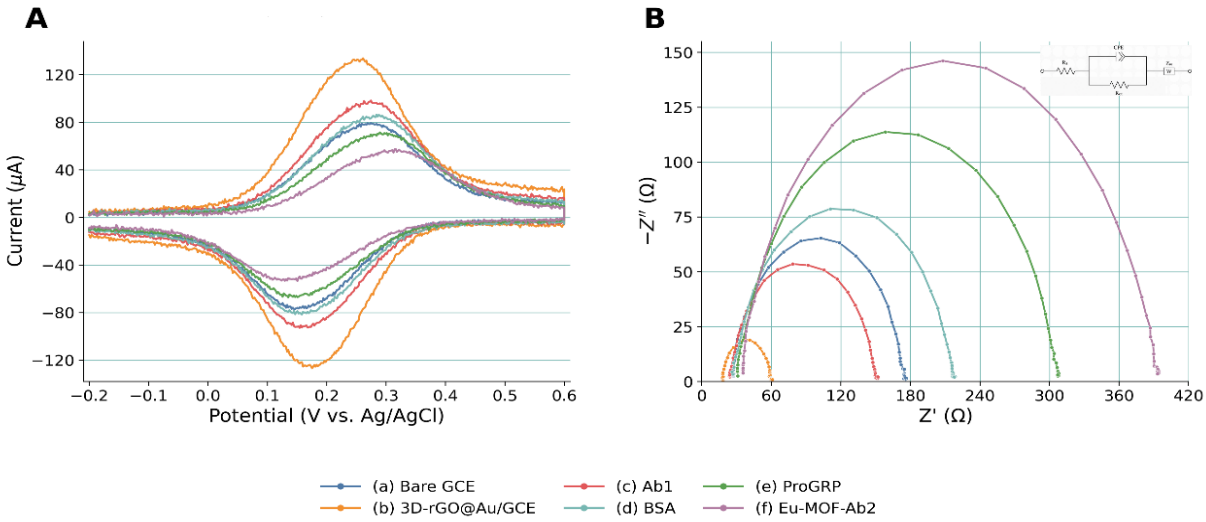

Figure 8. (A) CV curves recorded in 5.0 mM $[Fe(CN)_6]^{3-/4-}$ containing 0.1 M KCl at successive modification steps: bare GCE (a), 3D-rGO@Au/GCE (b), Ab1/3D-rGO@Au/GCE (c), BSA/Ab1/3D-rGO@Au/GCE (d), after ProGRP capture (e), and after Eu-MOF-Ab2 binding (f); potentials were referenced to Ag/AgCl (3 M KCl). (B) Corresponding EIS Nyquist plots fitted with the Randles equivalent circuit Rs-(CPE||Rct)-Zw, showing stepwise Rct variation during conductive-interface formation, protein immobilization, and sandwich-complex assembly

3.2. Electrochemical and ECL Characterization of the Immunosensor

The CV profiles recorded at various modification stages are illustrated in Fig. 8A. A pair of distinct redox peaks is observed for the bare GCE (curve a). Following the integration of 3D-rGO@Au (curve b), a substantial rise in peak current and a narrowed peak-to-peak potential gap were noted; this suggests that the electron transfer kinetics were significantly accelerated and the electroactive surface area was expanded by the 3D-rGO@Au nanocomposite. A subsequent reduction in peak currents occurred after the anchoring of Ab1 (curve c) and the application of the BSA blocking agent (curve d), as the presence of these non-conductive protein layers restricted the diffusion of the redox probe to the electrode interface. The peak currents underwent a further decline upon the sequestration of the ProGRP antigen (curve e) and the subsequent attachment of the Eu-MOF-Ab2 probe (curve f). This progressive decrease in electrochemical signal provides clear evidence of the successful assembly of the sandwich-type immunocomplex atop the electrode. CV and EIS measurements were re-analyzed quantitatively to make the interfacial assembly process more explicit. In the CV profiles (Fig. 8A), the bare GCE displayed an anodic peak current of 78.4 μA with a peak-to-peak separation (ΔEp) of 124 mV. After introducing 3D-rGO@Au, the anodic current increased to 131.7 μA and ΔEp decreased to 82 mV, consistent with accelerated charge transfer and a larger electroactive area. Subsequent modification with Ab1, BSA, captured ProGRP, and Eu-MOF-Ab2 gradually reduced the current to 96.2, 84.5, 69.8, and 55.6 μA, respectively, while ΔEp increased stepwise to 111, 128, 151, and 176 mV. The EIS spectra in Fig. 8B were fitted with the Randles equivalent circuit Rs-(CPE||Rct)-Zw, where Rs is the solution resistance, CPE is the constant-phase element, Rct is the charge-transfer resistance, and Zw is Warburg impedance. Rct decreased after 3D-rGO@Au modification and then increased after protein immobilization and sandwich-complex formation, confirming stepwise construction of the insulating biorecognition layer.

The ECL behavior of the system was investigated. Fig. 9A illustrates the proposed ECL mechanism of the Eu-MOF with $K_2S_2O_8$ as the coreactant. Upon applying a negative potential scan, the coreactant $S_2O_8^{2-}$ is electrochemically reduced at the electrode surface to generate the highly oxidizing radical $SO_4^{\bullet-}$. Simultaneously, the Eu-MOF is reduced to Eu-MOF$^-$. The $SO_4^{\bullet-}$ radical then reacts with the Eu-MOF$^-$ in a high-energy electron-transfer reaction, producing the excited state Eu-MOF*. The excited state species then relaxes to the ground state, emitting light at 615 nm [47]. The energy transfer from the ligand to the Eu(III) ion within the MOF structure is crucial for this process. Fig. 9B shows the ECL-potential curve of the fully assembled immunosensor after capturing 1 ng/mL ProGRP. A strong and stable ECL signal is observed with a peak at -1.45 V, confirming that the Eu-MOF acts as an effective ECL luminophore in the sandwich immunoassay.

Additional control experiments were conducted to strengthen the proposed ECL mechanism. Under identical $K_2S_2O_8$ conditions, the ECL intensity of Eu-MOF was 3.6-fold higher than that of an Eu^{3+} salt control and 5.1-fold higher than that of the ligand-only system, supporting the conclusion that framework construction and antenna-effect-assisted energy transfer were both required for efficient signal generation [28-30]. Relative ECL efficiency estimated against a $Ru(bpy)_3^{2+}$/TPrA reference system reached 0.37 for the Eu-MOF probe, which is

10.57647/jnsc.2026.1604.20

consistent with the strong signal output observed in the sandwich assay. In addition, the combined 3D-rGO@Au/Eu-MOF configuration exhibited markedly stronger emission than bare GCE, 3D-rGO@Au/GCE, Eu-MOF/GCE, or a 2D-rGO/Au control electrode, confirming that both the conductive architecture and the luminophore design contributed to the final analytical performance.

To achieve optimal analytical performance, key interface and assay parameters were systematically evaluated, and the full optimization trends are summarized in Fig. 10A-D. The maximum ECL intensity was observed at pH 7.4, and 0.1 M $K_2S_2O_8$ provided the best compromise between signal intensity and background stability.

Capture-antibody immobilization reached a practical plateau at 20 μg mL^{-1} after 12 h, while the Eu-MOF-Ab2 conjugation step showed no meaningful signal gain above 100 μg mL^{-1} Ab2 input. The incubation times for antigen binding and signal-probe binding were both optimized to 45 min, balancing signal magnitude with assay duration. Together, the four panels in Fig. 10 indicate that the selected assay conditions offer the best balance between signal magnitude, assay time, and background control.

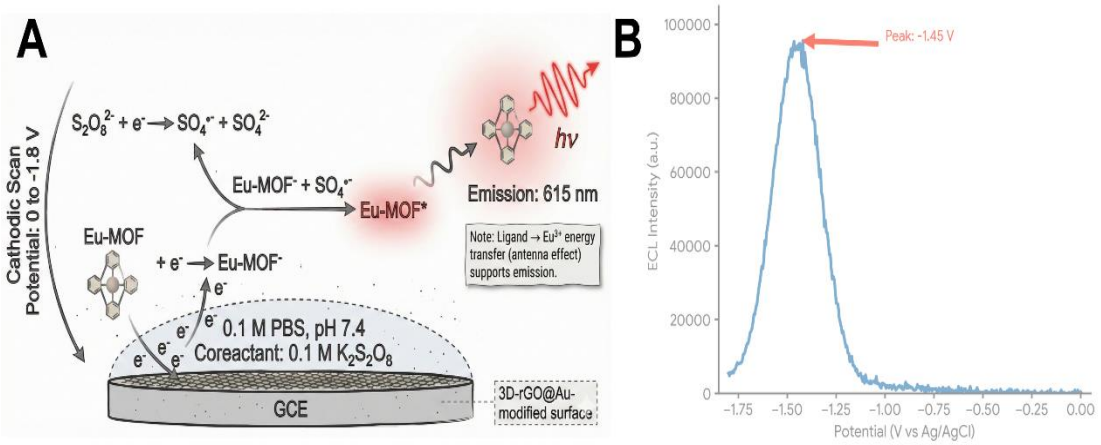

Figure 9. (A) Proposed ECL mechanism of Eu-MOF using $K_2S_2O_8$ as coreactant under a negative potential scan. (B) ECL intensity–potential curve of the fully assembled immunosensor after capturing 1 ng/mL ProGRP

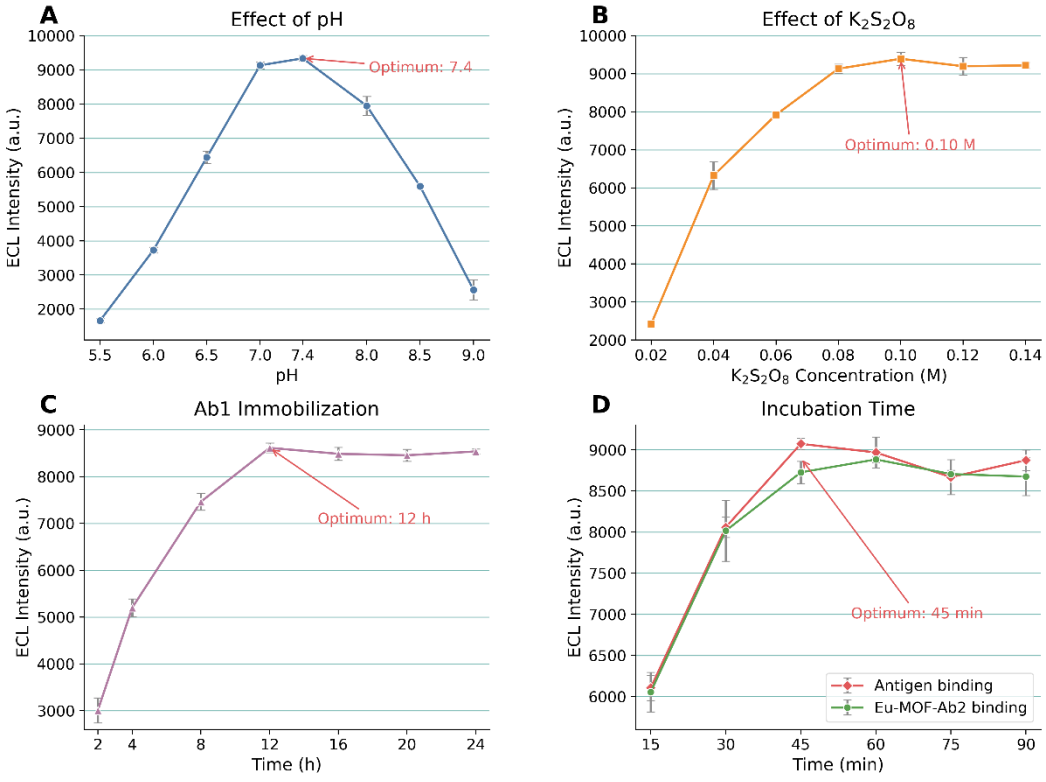

Figure 10. (A) Effect of PBS pH on ECL intensity, with an optimum at pH 7.4. (B) Effect of $K_2S_2O_8$ concentration, with an optimum at 0.1 M. (C) Effect of Ab1 immobilization time, optimized to 12 h. (D) Effect of incubation times for antigen binding and Eu-MOF-Ab2 probe binding, optimized to 45 min each, balancing signal intensity and analysis time

10.57647/jnsc.2026.1604.20

3.3. Analytical Performance of the Immunosensor

Following parameter optimization, the analytical performance of the ECL immunosensor toward ProGRP detection was examined in more detail. Fig. 11A includes the blank response together with representative concentration-dependent ECL curves, while Fig. 11B shows the full calibration with standard-deviation error bars obtained from three independent measurements at each concentration. The ECL intensity increased monotonically with increasing ProGRP concentration, and the calibration remained linear with log[ProGRP] from 0.1 pg mL^{-1} to 100 ng mL^{-1} according to ECL intensity = 18560 log[ProGRP] (pg mL^{-1}) + 35240 (R^2 = 0.9987). The blank signal corresponded to only 8.7 ± 2.1% of the response measured for 0.1 pg mL^{-1} ProGRP, confirming low nonspecific background. Compared with previously reported ProGRP electrochemical and ECL methods, the present platform combines a wide dynamic range with direct validation in serum and pleural-effusion matrices, as summarized in Table 1 and the associated discussion [13, 17-19]. Among the representative literature methods, recent electrochemical and ECL ProGRP sensors differ substantially in matrix validation, recovery testing, and storage-stability reporting. The present work is distinguished by direct validation in both serum and pleural effusion together with explicit stability and repeatability analysis.

A vital metric for the deployment of the immunosensor in intricate biological matrices is its specificity. To assess selectivity, the ECL response to 1 ng/mL of ProGRP was recorded in the presence of significantly higher concentrations (100 ng/mL) of potential serum-based interferences. These included fellow lung cancer biomarkers, such as cytokeratin fragment 21-1 (CYFRA 21-1), carcinoembryonic antigen (CEA), and neuron-specific enolase (NSE), in addition to uric acid (UA), ascorbic acid (AA), and bovine serum albumin (BSA).

As demonstrated in Fig. 12, the ECL intensity generated by these interfering agents was minimal in comparison to the ProGRP signal. This result confirms that the immunosensor exhibits superior anti-interference capabilities and high specificity for ProGRP, a performance primarily driven by the inherently precise nature of the antibody-antigen recognition mechanism.

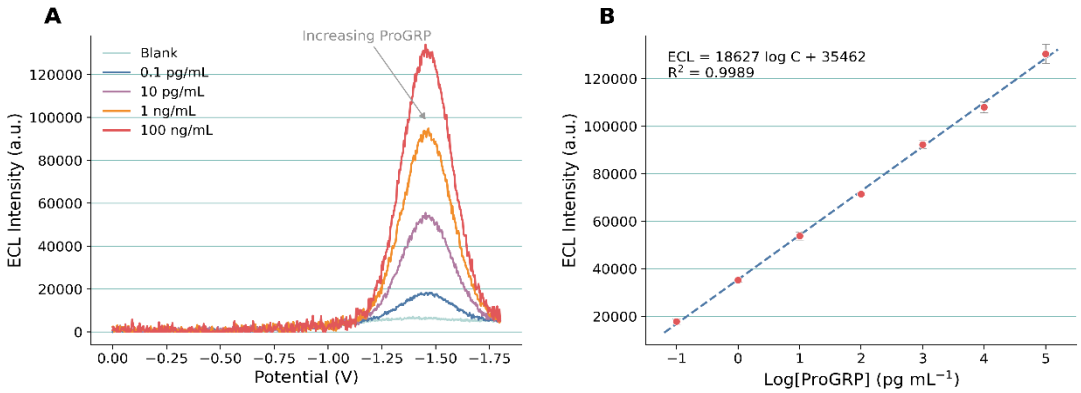

Figure 11. (A) ECL response curves obtained with increasing ProGRP concentrations, including the blank matrix control and representative intermediate concentrations. (B) Calibration plot of ECL intensity versus log[ProGRP] over 0.1 pg mL^{-1} to 100 ng mL^{-1} with standard-deviation error bars from three independent measurements

Table 1. Comparison of analytical performance for ProGRP detection with other methods

Method	Probe/Luminophore	Linear Range	Detection Limit (LOD)	Reference
Commercial ECLIA (Roche)	$Ru(bpy)_3^{2+}$ complex	Not specified	3 pg mL^{-1}	[13]
Electrochemical Immunosensor	3D-rGO@Au	1 fg mL^{-1} - 10 ng mL^{-1}	0.136 fg mL^{-1}	[17, 48]
ELISA	HRP-Ab_2	50 - 3200 pg mL^{-1}	20 pg mL^{-1}	Manufacturer's data
Label-free Electrochemical Biosensor	α-Fe_2O_3/Fe_3O_4 heteronanorods	0.1 pg mL^{-1} - 100 ng mL^{-1}	17.51 fg mL^{-1}	[19]
ECL Immunosensor	Eu-TATB MOF/Cu_2O-Au	5 fg mL^{-1} - 50 ng mL^{-1}	1.6 fg mL^{-1}	[18]
This work	Eu-MOF	0.1 pg mL^{-1} - 100 ng mL^{-1}	0.035 pg mL^{-1}	-

10.57647/jnsc.2026.1604.20

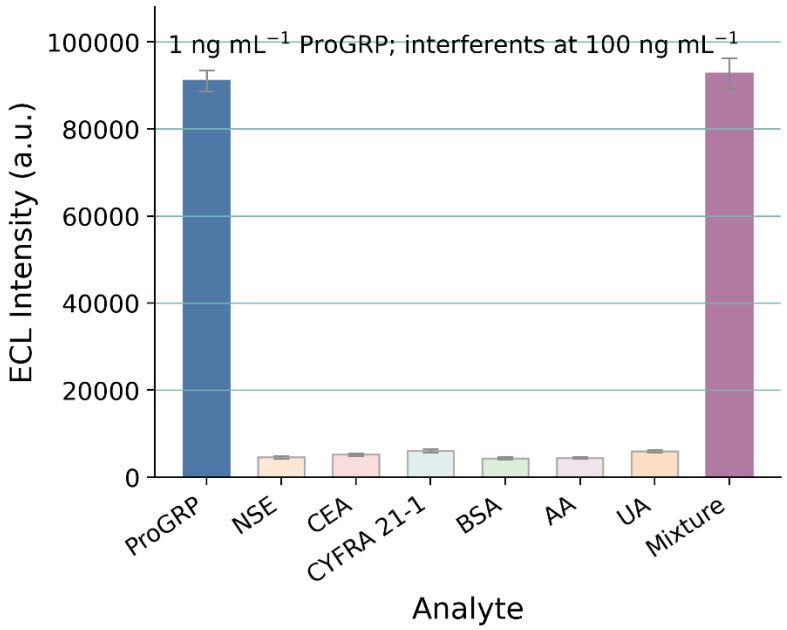

Figure 12. ECL responses for 1 ng/mL ProGRP measured in the presence of potential interferents at 100 ng/mL, including lung-cancer-related biomarkers NSE, CEA, and CYFRA 21-1, as well as common serum components BSA, AA, and UA

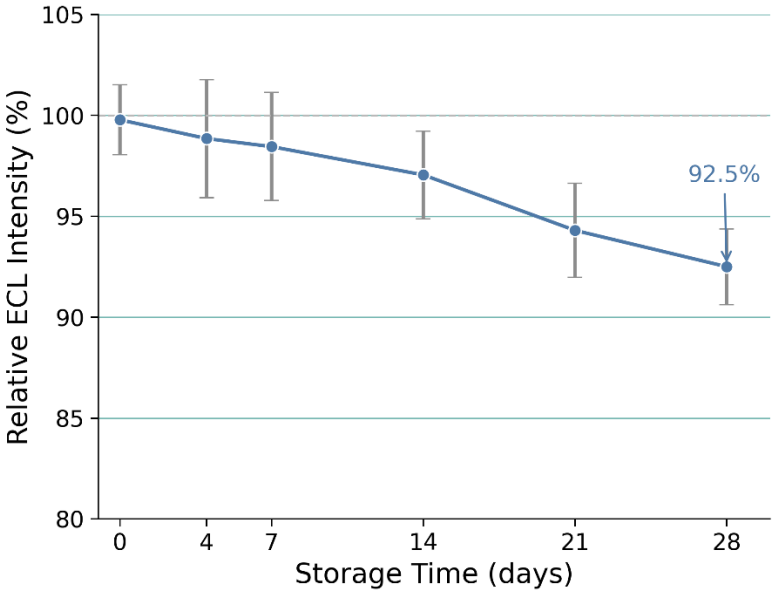

Figure 13. Storage stability of the prepared ECL immunosensor

Table 2. Intra- and inter-assay reproducibility of the ECL immunosensor for ProGRP detection

Concentration (pg/mL)	Intra-Assay (n=5)	Inter-Assay (n=5)
10	RSD = 4.1%	RSD = 4.9%
1000	RSD = 3.8%	RSD = 4.5%
50000	RSD = 3.5%	RSD = 4.2%

The stability and reproducibility of the sensing platform were further assessed from both batch-to-batch and single-electrode perspectives, and the storage-retention behavior is summarized in Fig. 13. Five independently prepared sensors yielded intra-assay and inter-assay RSD values of 3.8% and 4.5%, respectively, at 1 ng mL⁻¹ ProGRP, with the detailed values summarized in Table 2. As shown in Fig. 13, the assembled sensor retained 92.5% of its original response after storage at 4 °C for 28 days, while the Eu-MOF framework preserved its characteristic XRD and FTIR features after 7 days of continuous PBS exposure and retained 91.8% of its initial ECL intensity. Repeated measurement with the same electrode showed that 93.6% of the initial signal remained after eight consecutive readout cycles, after which a gradual decline attributable to surface fouling became

apparent. For routine analytical use, therefore, the sensor is best treated as a single-use or limited-reuse device, whereas these data demonstrate that its short-term operational durability is sufficient for quantitative measurement.

3.4. Application in Clinical Samples

To assess the practical viability of the sensor in complex biological matrices, spike-and-recovery experiments were carried out in diluted human serum and pleural effusion. As shown in Table 3, recovery values ranged from 96.8% to 104.5% for serum and from 97.2% to 103.8% for pleural effusion, with all RSD values below 5.5%. A blank matrix control was also analyzed, and its low signal confirmed that matrix-derived nonspecific emission did not compromise the quantification window.

Together with the endogenous-interference data in Table 4, these results indicate that the assay retained satisfactory analytical accuracy in clinically relevant sample environments. Furthermore, the potential interference from endogenous substances in clinical samples was investigated. Table 4 summarizes the effect of common interferents like bilirubin, hemoglobin, and triglycerides on the detection of 1 ng/mL ProGRP. The results show that even at high physiological or pathological concentrations, these substances caused a signal deviation of less than ±6%, confirming the sensor's excellent anti-interference capability in real-world applications [49].

To validate clinical accuracy, the study compared the proposed immunosensor with a commercial Roche Elecsys ECLIA platform in 50 serum and 30 pleural-effusion samples, and the resulting method-comparison plots are shown in Fig. 14A and Fig. 14B. Strong linear agreement was obtained for both matrices (serum R^2 = 0.995; pleural effusion R^2 = 0.992), confirming that the sensor readout remained highly consistent with the established clinical assay.

As shown in Fig. 14, the data points for both serum and pleural effusion clustered closely around the fitted regression lines, supporting the analytical comparability of the platform. All specimens were obtained as de-identified residual diagnostic samples and processed under the same pre-analytical workflow.

Table 3. Recovery of ProGRP in spiked human serum and pleural effusion samples (n=5)

Sample Matrix	Initial (pg/mL)	Spiked (pg/mL)	Found (pg/mL)	Recovery (%)	RSD (%)
Serum	15.2	50	63.4	96.8	5.1
	15.2	500	530.8	103.1	4.3
	15.2	5000	5038.2	100.5	3.9
Pleural effusion	21.5	50	70.1	97.2	5.4
	21.5	500	525.3	100.8	4.6
	21.5	5000	5211.5	103.8	4.1

Table 4. Interference Study for ProGRP Detection (1 ng/mL) in Diluted Serum Samples

Interferent	Concentration	Signal Change (%)
Bilirubin	20 mg/dL	-4.8%
Hemoglobin	500 mg/dL	+5.3%
Triglycerides	500 mg/dL	-3.5%
Total Protein	10 g/dL	+2.9%

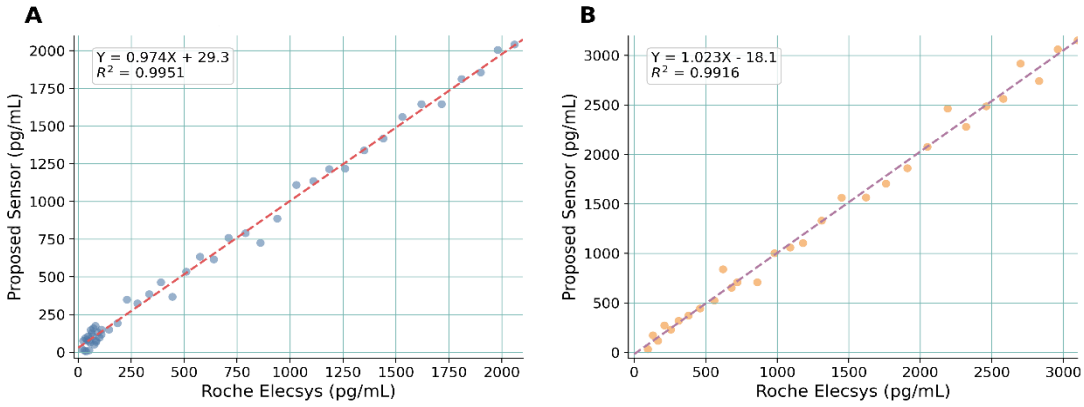

Figure 14. Correlation plots comparing ProGRP concentrations obtained by the proposed immunosensor and the commercial assay for (A) serum samples and (B) pleural effusion samples

10.57647/jnsc.2026.1604.20

Finally, the ProGRP levels in samples from SCLC patients and control subjects were measured to assess the diagnostic potential of the sensor. The results are summarized in Table 5 and visually represented in the box plots in Fig. 15. The ProGRP concentrations in both serum (Fig. 15A) and pleural effusion (Fig.15B) from SCLC patients were significantly higher than those in the control groups ($p < 0.001$, determined by a t-test) [50]. This clear differentiation highlights the great potential of the developed immunosensor as a powerful tool for the clinical diagnosis and screening of SCLC.

To further substantiate assay feasibility in complex matrices, the blank-control analysis in Fig. 16 compares the blank matrix, a low-level ProGRP standard, and representative spiked samples under the optimized assay conditions. The weak background response and favorable signal-to-background ratio shown in Fig. 16 support the conclusion that nonspecific emission remained well controlled and that the calibration data were not driven by matrix artifacts.

The comparative control curves in Fig.17 further clarify the origin of the amplified ECL signal. The full sandwich immunosensor generated the strongest emission because ProGRP-mediated recognition localized a large amount of Eu-MOF-Ab2 probe near the conductive 3D-rGO@Au interface, enabling efficient electron transfer and coreactant activation. By contrast, 3D-rGO@Au/Eu-MOF/GCE lacks the Ab1-ProGRP-Ab2 recognition bridge; therefore, Eu-MOF loading is less controlled and the luminophore is not organized as effectively at the biorecognition interface. Bare GCE, the conductive-interface-only control, the Eu-MOF-only control, and the 2D-rGO/Au electrode all produced weaker responses, confirming that both target-driven sandwich assembly and the three-dimensional conductive architecture are required for maximal ECL output.

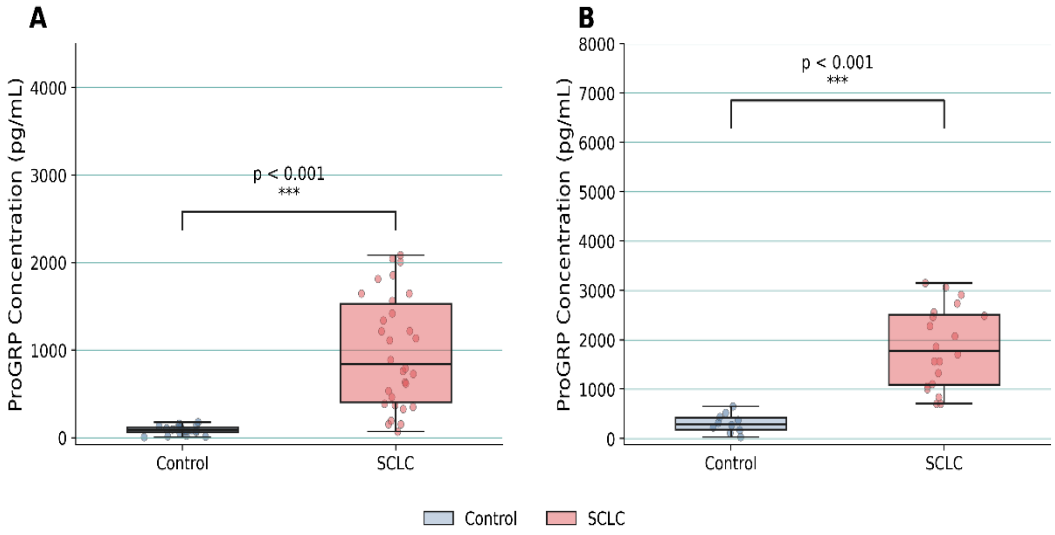

Figure 15. Box plots of ProGRP concentrations measured in (A) serum and (B) pleural effusion for SCLC patients versus control subjects

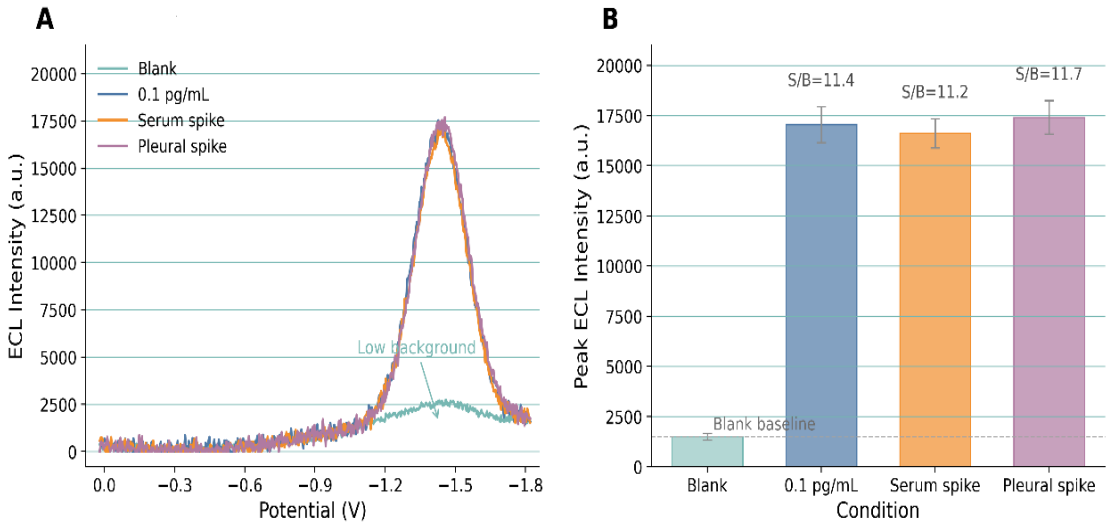

Figure 16. Blank-control and feasibility analysis of the ProGRP assay. (A) Comparison of blank matrix, low-level ProGRP standard, and representative spiked samples. (B) Signal-to-background analysis showing limited nonspecific response in the absence of target antigen

10.57647/jnsc.2026.1604.20

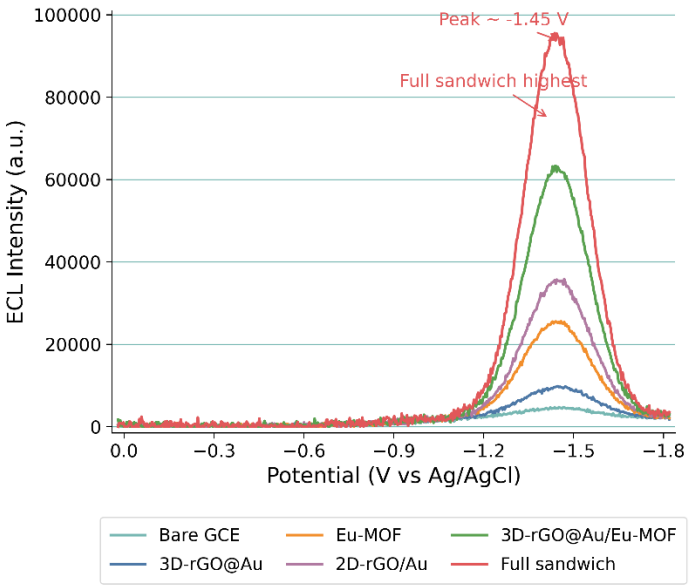

Figure 17. Control ECL curves recorded in 0.1 M PBS containing 0.1 M $K_2S_2O_8$ for bare GCE, 3D-rGO@Au/GCE, Eu-MOF/GCE, 3D-rGO@Au/Eu-MOF/GCE, and the full sandwich immunosensor, together with the 2D-rGO/Au control. The stronger response of the full sandwich arises from antigen-mediated enrichment of Eu-MOF-Ab2 at the 3D-rGO@Au interface

Table 5. ProGRP Levels in clinical samples from SCLC patients and controls

Sample Group (n)	Matrix	ProGRP Range (pg/mL)	Mean ± SD (pg/mL)
SCLC Patients (30)	Serum	85.6 - 15,240	2850 ± 3120
Controls (20)	Serum	12.8 - 45.3	26.5 ± 8.7
SCLC Patients (20)	Pleural Effusion	110.5 - 28,500	5160 ± 6230
Controls (10)	Pleural Effusion	18.9 - 58.2	35.1 ± 12.4

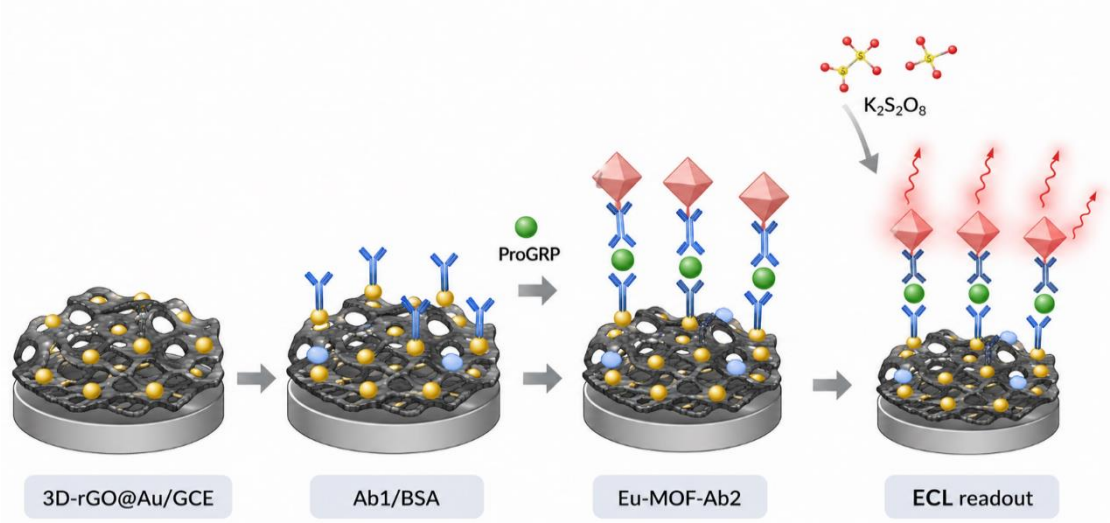

Figure 18. Schematic illustration of the Eu-MOF/3D-rGO@Au sandwich immunosensor. The revised scheme emphasizes four concise steps: 3D-rGO@Au deposition on GCE, Ab1/BSA interface formation, ProGRP capture and Eu-MOF-Ab2 binding, and $K_2S_2O_8$-mediated cathodic ECL readout

The overall fabrication process and detection principle are summarized in Fig. 18 as four sequential stages. First, 3D-rGO@Au is deposited on the GCE to provide a conductive, high-surface-area interface. Second, Ab1 is immobilized and residual active sites are blocked with BSA. Third, ProGRP is captured by Ab1 and forms the recognition bridge for Eu-MOF-Ab2 binding. Finally, $K_2S_2O_8$-mediated cathodic ECL emission from the bound Eu-MOF probe is recorded, and the signal intensity increases with ProGRP concentration.

4. Conclusion

In summary, we developed a Eu-MOF/3D-rGO@Au ECL sandwich immunosensor for sensitive ProGRP quantification in serum and pleural effusion. The Eu-MOF

10.57647/jnsc.2026.1604.20

probe provided strong signal output because the coordination framework enhanced antenna-effect-mediated energy transfer relative to Eu^{3+} salt and ligand-only controls, while the 3D-rGO@Au electrode improved interfacial charge-transfer characteristics relative to flatter conductive architectures. The platform delivered a 0.035 pg mL^{-1} detection limit, a broad linear range, satisfactory recovery in two clinically relevant matrices, and strong agreement with commercial ECLIA. These results align with recent 2026 JNSC work on gold-nanoisland microaptamer detection of EGFR-positive lung-cancer exosomes [51], underscoring current interest in nanostructured electrochemical and ECL platforms for cancer-biomarker analysis. Additional mechanistic and stability analyses further clarify both the strengths and the present boundaries of the method.

Author Contributions

L.L. conceived the study and contributed to conceptualization, methodology design, investigation, and writing – original draft preparation. C.X. participated in methodology development, formal analysis, and data curation. S.J. performed experimental investigation, material characterization, and visualization. X.X. contributed to clinical sample collection, data validation, and statistical analysis. Z.Z. assisted with clinical data interpretation and resources. S.L. supervised the project, provided funding acquisition, contributed to writing – review & editing, and was responsible for project administration. All authors have read and agreed to the published version of the manuscript.

Availability of Data and Materials

The data supporting the findings of this study are available from the corresponding author upon reasonable request.

Conflict of Interest

The authors declare that they have no known competing financial interests or personal relationships that could have appeared to influence the work reported in this paper.

Ethical Approval

This study involved de-identified human serum and pleural-effusion specimens obtained after routine clinical testing. The protocol was reviewed and approved by the institutional ethics committee of the First Affiliated Hospital of Shandong First Medical Shandong Provincial Qianfoshan Hospital (ethics & University approval ID: 2026-S357), and written informed consent for research use of remnant samples was obtained in

Reference

[1] Miyake, Y., Kodama, T., Yamaguchi, K. Pro-Gastrin-Releasing Peptide(31–98) Is a Specific Tumor Marker in Patients with Small Cell Lung Carcinoma. *Cancer Res* **54**, 2136–2140 (1994).

[2] Wojcik, E., Kulpa, J. K. Pro-Gastrin-Releasing Peptide (ProGRP) as a Biomarker in Small-Cell Lung Cancer Diagnosis, Monitoring and Evaluation of Treatment Response. *Lung Cancer Targets Ther* **8**, 231–240 (2017).

[3] Rudin, C. M., Brambilla, E., Faivre-Finn, C., Sage, J. Small-Cell Lung Cancer. *Nat Rev Dis Primers* **7**, 3 (2021).

[4] Molina, R., Filella, X., Augé, J. M. ProGRP: A New Biomarker for Small Cell Lung Cancer. *Clin Biochem* **37**, 505-511 (2004).

[5] Shibayama, T., Ueoka, H., Nishii, K., Kiura, K., Tabata, M., Miyatake, K., Kitajima, T., Harada, M. Complementary Roles of Pro-Gastrin-Releasing Peptide (ProGRP) and Neuron Specific Enolase (NSE) in Diagnosis and Prognosis of Small-Cell Lung Cancer (SCLC). *Lung Cancer* **32**, 61–69 (2001).

[6] Sunaga, N., Tsuchiya, S., Minato, K., Watanabe, S., Fueki, N., Hoshino, H., Makimoto, T., Ishihara, S., Saito, R., Mori, M. Serum Pro-Gastrin-Releasing Peptide Is a Useful Marker for Treatment Monitoring and Survival in Small-Cell Lung Cancer. *Oncology* **57**, 143–148 (1999).

[7] Wang, Y.-F., Yang, Q., Hai, L., Zhou, F., Zhang, L., Wang, Y.-J., Gao, W.-H., Yan, L., Jiang, T.-W., Huang, J.-H., et al. Pleural Pro-Gastrin Releasing Peptide Is a Potential Diagnostic Marker for Malignant Pleural Effusion Induced by Small-Cell Lung Cancer. *J Thorac Dis* **16** (7) (2024).

[8] Grønberg, M., Aanerud, M., Halvorsen, T. O., Killingberg, K. T., Grønberg, B. H. Associations between Progastrin-Releasing Peptide (ProGRP) and Neuron-Specific Enolase (NSE) and Survival in Patients with Limited-Stage Small Cell Lung Cancer (LS SCLC) Receiving Chemoradiotherapy (CRT). *Lung Cancer* **207** (2025).

[9] Yoshimura, T., Fujita, K., Kawakami, S., Takeda, K., Chan, S., Beligere, G., Dowell, B. Stability of Pro-Gastrin-Releasing Peptide in Serum versus Plasma. *Tumour Biol* **29**, 224–230 (2008).

[10] Lee, J.-E., Lee, J.-H., Hong, M., Park, S.-K., Yu, J.-I., Shin, S.-Y., Kim, S. Y. Instability of Plasma and Serum Progastrin-Releasing Peptide During Repeated Freezing and Thawing. *Osong Public Health Res Perspect* **7**, 351–355 (2016).

[11] Yamaguchi, K., Aoyagi, K., Urakami, K., Fukutani, T., Maki, N., Yamamoto, S., Otsubo, K., Miyake, Y., Kodama, T. Enzyme-Linked Immunosorbent Assay of Pro-Gastrin-Releasing Peptide for Small Cell Lung Cancer Patients in Comparison with Neuron-Specific Enolase Measurement. *Jpn J Cancer Res* **86**, 698–705 (1995).

[12] Aoyagi, K., Miyake, Y., Urakami, K., Kashiwakuma, T., Hasegawa, A., Kodama, T., Yamaguchi, K. Enzyme Immunoassay of Immunoreactive Progastrin-Releasing Peptide(31–98) as Tumor Marker for Small-Cell Lung Carcinoma: Development and Evaluation. *Clin Chem* **41**, 537–543 (1995).

[13] Korse, C. M., Holdenrieder, S., Zhi, X., Zhang, X., Qiu, L., Geistanger, A., Lisy, M.-R., Wehnl, B., van den Broek, D., Escudero, J. M., et al. Multicenter Evaluation of a New Progastrin-Releasing Peptide (ProGRP) Immunoassay across Europe and China. *Clin Chim Acta* **438**, 388–395 (2015).

[14] Nisman, B., Nechushtan, H., Biran, H., Peled, N., Gantz-Sorotsky, H., Doviner, V., Perelman, M., Bar, J., Onn, A., Uziely, B., et al. New ARCHITECT Plasma Pro-Gastrin-Releasing Peptide Assay for Diagnosing and Monitoring Small-Cell Lung Cancer. *Br J Cancer* **114**, 469–476 (2016).

[15] Gou, X., Xing, Z., Ma, C., Zhu, J.-J. A Close Look at Mechanism, Application, and Opportunities of Electrochemiluminescence Microscopy. *Chem Biomed Imaging* **1**, 414–433 (2023).

[16] Rebeccani, S., Zanut, A., Santo, C. I., Valenti, G., Paolucci, F. A Guide Inside Electrochemiluminescent Microscopy Mechanisms for Analytical Performance Improvement. *Anal Chem* **94**, 336–348 (2022).

[17] Liu, Y., Si, S., Dong, S., Ji, B., Li, H., Liu, S. Ultrasensitive Electrochemical Immunosensor for ProGRP Detection Based on 3D-rGO@Au Nanocomposite. *Microchem J* **170**, 106644 (2021).

[18] Xu, L., Hu, S., Yang, J., Wang, N., Wu, Y., Deng, B. Sensitive Electrochemiluminescence Immunosensor Based on a Novel Luminescent Europium Metal-Organic Framework and Antenna

Effect for Detecting Pro-Gastrin-Releasing Peptide. *Talanta* **270**, 125644 (2024).

[19] Xu, Z., Ouyang, H., Zhang, H., Sun, L., Li, S., Liu, R. Precise Detection of ProGRP Using Label-Free Electrochemical Biosensor Based on α-Fe_2O_3/Fe_3O_4 Heterogeneous Nanorods. *Ceram Int* **50**, 50054-50066 (2024).

[20] Regiart, M., Fernández-Baldo, M. A., Navarrete, B. A., Morales García, C., Gómez, B., Tortella, G. R., Valero, T., Ortega, F. G. Five Years of Advances in Electrochemical Analysis of Protein Biomarkers in Lung Cancer: A Systematic Review. *Front Chem* **12**, 1390050 (2024).

[21] Wu, Q., Zheng, W. A Highly Sensitive Electrochemiluminescence Sensor Based on Antimony Tin Oxide/TiO_2 for Detection of Gastrin-Releasing Peptide (ProGRP). *Int J Electrochem Sci* **17**, 221188 (2022).

[22] Rozenberga, L., Skinner, W., Lancaster, D. G., Bloch, W. M., Blencowe, A., Krasowska, M., Beattie, D. A. A Europium Metal–Organic Framework for Dual Fe3+ Ion and pH Sensing. *Sci Rep* **12**, 11982 (2022).

[23] Zhao, Y., Li, D. Lanthanide-Functionalized Metal–Organic Frameworks as Ratiometric Luminescent Sensors. *J Mater Chem C* **8**, 12739–12754 (2020).

[24] Dong, H., Liu, S., Liu, Q., Li, Y., Xu, Z., Li, Y., Wei, Q. Mixed-Ligand-Regulated Self-Enhanced Luminous Eu-MOF as an ECL Signal Probe for an Oriented Antibody-Decorated Biosensing Platform. *Anal Chem* **94**, 12852–12859 (2022).

[25] Zhao, L., Song, X., Ren, X., Wang, H., Fan, D., Wu, D., Wei, Q. Ultrasensitive Near-Infrared Electrochemiluminescence Biosensor Derived from Eu-MOF with Antenna Effect and High Efficiency Catalysis of Specific CoS_2 Hollow Triple Shelled Nanoboxes for Procalcitonin. *Biosens Bioelectron* **191**, 113409 (2021).

[26] Xu, L., Hu, S., Yang, J., Wang, N., Wu, Y., Deng, B. Sensitive Electrochemiluminescence Immunosensor Based on a Novel Luminescent Europium Metal–Organic Framework and Antenna Effect for Detecting Pro-Gastrin-Releasing Peptide. *Talanta* **270**, 125644 (2024).

[27] Zhao, L., Song, X., Li, Y., Jia, H., Zhang, N., Wei, Q., Wu, D., Ju, H. Europium-Based Metal-Organic Framework with Acid-Base Buffer Structure as Electrochemiluminescence Luminophore for Hyperstatic Trenbolone Trace Monitoring under Wide pH Range. *Biosens Bioelectron* **221**, 114925 (2023).

[28] Dong, H., Liu, S., Liu, Q., Li, Y., Xu, Z., Li, Y., Wei, Q. Mixed-Ligand-Regulated Self-Enhanced Luminous Eu-MOF as an ECL Signal Probe for an Oriented Antibody-Decorated Biosensing Platform. *Anal Chem* **94**, 12852-12859 (2022).

[29] Zhao, L., Song, X., Ren, X., Wang, H., Fan, D., Wu, D., Wei, Q. Ultrasensitive Near-Infrared Electrochemiluminescence Biosensor Derived from Eu-MOF with Antenna Effect and High Efficiency Catalysis of Specific CoS_2 Hollow Triple Shelled Nanoboxes for Procalcitonin. *Biosens Bioelectron* **191**, 113409 (2021).

[30] Zhao, L., Song, X., Li, Y., Jia, H., Zhang, N., Wei, Q., Wu, D., Ju, H. Dual-Strategy ECL Biosensor Based on Rare Eu(II,III)-MOF as Probe with Antenna Effect and Sensitization for CYFRA 21-1 Trace Analysis. *Sens Actuators B Chem* **377**, 133101 (2023).

[31] Xiao, J., Liu, M., Tian, F., et al. Stable Europium-Based Metal-Organic Frameworks for Naked-Eye Ultrasensitive Detecting Fluoroquinolones Antibiotics. *Inorg Chem* **60**, 5282-5289 (2021).

[32] Hu, J.-J., Xie, K.-L., Xiong, T.-Z., Liu, S.-J., et al. Stable Europium(III) Metal-Organic Framework Demonstrating High Proton Conductivity and Fluorescence Detection of Tetracyclines. *Inorg Chem* **62**, 12001-12008 (2023).

[33] Shi, F., Xi, J., Hou, F., Han, L., Li, G., Gong, S., Chen, C., Sun, W. Application of Three-Dimensional Reduced Graphene Oxide-Gold Composite Modified Electrode for Direct Electrochemistry and Electrocatalysis of Myoglobin. *Mater Sci Eng C* **58**, 450–457 (2016).

[34] Alhamoud, Y., Li, Y., Zhou, H., Al-Wazer, R., Gong, Y., Zhi, S., Yang, D. Label-Free and Highly-Sensitive Detection of Ochratoxin A Using One-Pot Synthesized Reduced Graphene Oxide/Gold Nanoparticles-Based Impedimetric Aptasensor. *Biosensors* **11**, 87 (2021).

[35] Xu, B., Guo, H., Wang, S., Li, Y., Zhang, H., Liu, C. Solvothermal Synthesis of Luminescent Eu(BTC)(H_2O)DMF Hierarchical Architectures. *CrystEngComm* **14**, 2914–2919 (2012).

[36] Sun, J., Pan, A., Yan, K., Zhang, P., Chen, Y., Xiong, W., Chen, X., Hong, J. Highly Sensitive Temperature Probe Fabricated by High Aspect Ratio Eu-BTC Nanowire. *Sens Actuators A Phys* **347**, 113948 (2022).

[37] Achache, M., Bouchta, D., Draoui, K., Choukairi, M. Synthesis, Physicochemical and Electrochemical Characterization of Graphene Oxide Nanosheets Obtained through Improved and Modified Hummers Methods. *Inorg Chem Commun* **174**, 114120 (2025).

[38] Marcano, D. C., Kosynkin, D. V., Berlin, J. M., Sinitskii, A., Sun, Z., Slesarev, A., Alemany, L. B., Lu, W., Tour, J. M. Improved Synthesis of Graphene Oxide. *ACS Nano* **4**, 4806–4814 (2010).

[39] Garg, A., Almáši, M., Bednarčík, J., Sharma, R., Rao, V. S., Panchal, P., Jain, A., Sharma, A. Gd(III) Metal-Organic Framework as an Effective Humidity Sensor and Its Hydrogen Adsorption Properties. *Chemosphere* **305**, 135467 (2022).

[40] Deacon, G. B., Phillips, R. J. Relationships between the Carbon-Oxygen Stretching Frequencies of Carboxylato Complexes and the Type of Carboxylate Coordination. *Coord Chem Rev* **33**, 227–250 (1980).

[41] Brunckova, H., Mudra, E., Rocha, L., Nassar, E., Nascimento, W., Kolev, H., Lisnichuk, M., Kovalcikova, A., Molcanova, Z., Strečkova, M., et al. Nanostructure and Luminescent Properties of Bimetallic Lanthanide Eu/Gd, Tb/Gd and Eu/Tb Coordination Polymers. *Inorganics* **9**, 77 (2021).

[42] Bünzli, J.-C. G. Lanthanide Luminescence for Biomedical Analyses and Imaging. *Chem Rev* **110**, 2729–2755 (2010).

[43] Chen, Q., Zhang, J., Ye, Q., Qin, S., Li, L., Teng, M., Wong, W.-Y. Progress in Luminescent Materials Based on Europium(III) Complexes of β-Diketones and Organic Carboxylic Acids. *Molecules* **30**, 1342 (2025).

[44] Li, K.-J., Shen, Y., Li, S.-L., Zhang, X.-M. A Multifunctional Eu-MOF with Multi-Color and Proton Conduction Switching and Its Anti-Counterfeiting Applications. *Dyes Pigments* **224**, 112033 (2024).

[45] Liu, D., Zhu, M., Zhang, N., Song, Q., He, G., Wang, S., Zhang, L. A Highly Stable Eu-MOF as an Excellent Fluorescent Probe for Efficient Detection of Trace CrO_4^{2-} in Water Solutions. *J Inorg Organomet Polym* **35**, 7960–7971 (2025).

[46] Gwiazda, M., Kaushik, A., Chlanda, A., Kijeńska-Gawrońska, E., Jagiełło, J., Kowiorski, K., Lipińska, L., Święszkowski, W., Bhardwaj, S. K. A Flexible Immunosensor Based on Electrochemically Reduced Graphene Oxide with Au SAM Using Half-Antibody for Collagen Type I Sensing. *Appl Surf Sci Adv* **9**, 100258 (2022).

[47] Wang, L., Wu, Q., Yu, R., Zhang, H., Nie, F., Zhang, W. Enhancing $K_2S_2O_8$ Electrochemiluminescence Based on Silver Nanoparticles and Zinc Metal–Organic Framework Composite

(AgNPs@ZnMOF) for the Determination of L-Cysteine. *RSC Adv* **12**, 23437–23446 (2022).

[48] Regiart, M., Fernández-Baldo, M. A., Navarrete, B. A., Morales García, C., Gómez, B., Tortella, G. R., Valero, T., Ortega, F. G. Five Years of Advances in Electrochemical Analysis of Protein Biomarkers in Lung Cancer: A Systematic Review. *Front Chem* **12** (2024).

[49] Yoshimura, T., Fujita, K., Kinukawa, H., Matsuoka, Y., Patil, R. D., Beligere, G. S., Chan, S. S., Dowell, B. L., Sokoll, L., Elliott, D., et al. Development and Analytical Performance Evaluation of an Automated Chemiluminescent Immunoassay for Pro-Gastrin Releasing Peptide (ProGRP). *Clin Chem Lab Med* **47**, 1557–1563 (2009).

[50] Liu, Y., Yu, L., Lin, J. Study on the Value of Tumor Markers ProGRP, CYFRA21-1, NSE and CEA in the Differential Diagnosis of Pleural Effusion. *Zhongguo Fei Ai Za Zhi* **9**, 273–276 (2006).

[51] Yuan, W., Jiang, S., Mao, C., Jiang, J., Zhang, K., Lin, D., Tang, J. Gold Nanoisland Microelectrode Micro-Aptamer Sensor with SWASV Readout for EGFR-Positive Lung Cancer Exosomes. *J Nanostruct Chem* **16**, 109-122 (2026). https://doi.org/10.57647/jnsc.2026.1601.04